Site Occupancy of Ti^{4+}-Doped $ZrGeO_4$ and $HfGeO_4$ Probed by Raman Spectroscopy

David D. Tuschel* and Patrick M. Lambert

Eastman Kodak Company, Rochester, New York, 14650-2017

Received April 10, 1997. Revised Manuscript Received August 11, 1997[⊗]

Isostructural $HfGeO_4$ and $ZrGeO_4$, activated with Ti^{4+}, yield blue luminescence when irradiated with X-rays. An adequate understanding of the observed blue luminescence requires the determination of the site occupancy and the local Ti^{4+} environment; i.e., the site symmetry. Raman spectroscopy has been used to probe the chemical bonding and crystal structure of metal germanates. The group vibrational modes of $MGeO_4$ (M = Zr, Hf) are assigned through shifts of the Raman bands in a $Hf_{1-x}Zr_xGeO_4$ solid solution series and through the application of the Raman polarization selection rules to micro-Raman spectra of single crystals. Macro-Raman spectra of undoped and titanium-activated $ZrGeO_4$ and $HfGeO_4$ powder samples and micro-Raman spectra of single crystals of $ZrGeO_4$:Ti^{4+} confirm that Ti^{4+} occupies the Ge^{4+} site in $ZrGeO_4$ and in $HfGeO_4$. In addition, not all of the GeO_4^{4-} modes are strongly affected by Ti^{4+} doping, even though all of the modes most affected by Ti^{4+} doping arise from the GeO_4^{4-} group. It is observed that Ti^{4+} substitution for Ge^{4+} significantly affects Raman bands arising from GeO_4^{4-} rotational and bending motions about the *c*-axis, within the *ab*-plane.

Introduction

Under X-ray irradiation, $HfGeO_4$ exhibits a strong ultraviolet emission,[1] and, upon activation with Ti^{4+}, a broad blue luminescence centered at 425 nm is observed.[2] The high X-ray absorption of the material (ρ = 8.5 g/cm^3), in combination with efficient luminescence, establishes the compound as a promising X-ray phosphor. Hafnium and zirconium germanate crystallize in the scheelite structure (Figure 1). Chains of eight-coordinate Hf^{4+} cations traverse the *ab*-plane in the directions of the respective axes, while isolated GeO_4^{4-} tetrahedra alternate with the Hf^{4+} cations in the *c* direction. The GeO_4^{4-} moieties are distorted; exhibiting compression in the *c* direction. An adequate understanding of the observed blue luminescence requires the determination of the local titanium environment, i.e., the site symmetry. Lattice parameter and elemental analyses of compositions in $HfGeO_4$:Ti^{4+} solid solution indirectly suggest that the bulk of the Ti^{4+} activator resides at the tetrahedral site.[3]

Zircon, $ZrSiO_4$, is related structurally to scheelite phases of $HfGeO_4$ and $ZrGeO_4$ in that each contain only 8-fold and 4-fold coordination spheres. The distinction between the structures lies in the three-dimensional linkage of the two sites. The site symmetry of impurities in the zircon phase has been examined by ESR and electronic spectroscopy with considerable effort directed to the location of V^{4+}.[4−6] Andres et al.[7] and Beltran et al.[8] applied ab initio perturbed ion calculations to propose that V^{4+} lies in the eight-coordinate site in $ZrSiO_4$. Chandley et al.[9] used lattice-energy calculations, electron microprobe, and X-ray diffraction to conclude that V^{4+} resides at both the tetrahedral and 8-fold sites in $ZrSiO_4$ but only at the tetrahedral site in $ZrGeO_4$. The authors also suggest that Tb^{4+} dopes into the Zr^{4+} site in $ZrGeO_4$. In a subsequent paper, Andres et al. extended their ab initio perturbed-ion modeling to V^{4+} and Tb^{4+} in $ZrGeO_4$.[10] Pope and West summarized the FT Raman spectra of a number of inorganic tetrahedral ions over the temperature range 77−473 K.[11]

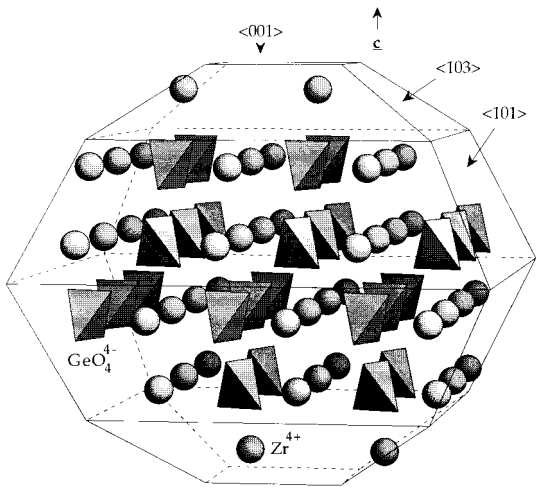

Figure 1. Habit and crystal structure of $MGeO_4$.

[⊗] Abstract published in *Advance ACS Abstracts,* October 1, 1997.

(1) Lambert, P. M.; Bryan, P. S.; Jarrold, G. S.; Towers, C. M. U.S. Patent 5,173,611.
(2) Lambert, P. M.; Bryan, P. S.; Jarrold, G. S.; Towers, C. M. U.S. Patent 5,112,700.
(3) Lambert, P. M.; Jarrold, G. S.; Towers, C. M.; Tuschel, D. D.; McMillan, M. 188th Electrochemical Society Meeting, Chicago, Oct 1995.
(4) Demiray, T.; Nath D. K.; Hummel, F. A. *J. Am. Ceram. Soc.* **1970**, *53*, 1.
(5) Di Gregorio, S.; Greenblatt, M.; Pifer, J. H.; Sturge, M. D. *J. Chem. Phys.* **1982**, *76*, 2931.
(6) Xiaoyo, H.; Gui-ru, B.; Min-guang, Z. *J. Phys. Chem. Solids* **1985**, *46*, 719.
(7) Andrés, J.; Beltrán, A.; Carda, J.; Monrós, G. *Int. J. Quantum Chem. Symp.* **1993**, *27*, 175.
(8) Beltrán, A.; Bohm, S.; Flores-Riveros, A.; Igualada, J. A.; Monrós, G.; Andrés, J. *J. Phys. Chem.* **1993**, *97*, 1555.
(9) Chandley, P.; Clark, R. J. H.; Angel, R. J.; Price, G. D. *J. Chem. Soc., Dalton Trans.* **1992**, 1579.
(10) Andrés, J.; Beltrán, A.; Llusar, R. *Chem. Phys. Lett.* **1995**, *236*, 521.

S0897-4756(97)00205-6 CCC: $14.00

A convenient method for probing the chemical bonding and crystal structure of metal oxides is Raman spectroscopy. Early studies of compounds having the scheelite structure, such as $CaWO_4$, $SrWO_4$, $CaMoO_4$, and $SrMoO_4$, demonstrated that Raman bands could be reasonably assigned to internal and external lattice vibrational modes.[12,13] The distinction pertains, in this case, to the vibrational motions of the isolated transition metal−oxide tetrahedra. Those vibrational motions of the tetrahedra in which the center of mass does not move are regarded as internal modes; i.e., the vibrational motions approximate those of an isolated tetrahedron. In contrast, external modes are assigned to translational movement of the metal cation or tetrahedron or rotational motion of the tetrahedron. More recently, work has been performed on scheelite tungstates relating the wavenumbers of internal stretching modes to W−O bond strengths and lengths.[14] Raman polarization selection rules, in conjunction with internal and external mode assignments, have been applied to study the effects of mixed cations on bonding and crystal structure in $M^{I}M^{III}(XO_4)_2$ compounds.[15−17] Raman spectroscopy has been used to study the scheelite crystal $LiYF_4$, which is of technological interest as a laser host crystal for lanthanides.[18] A Raman study of Nd^{3+}-doped $GdLiF_4$ and $YLiF_4$ has been performed, but the authors did not report any effects of Nd^{3+} doping on the lattice vibrational modes.[19]

Previous studies of metal germanates by vibrational (Raman and infrared) spectroscopies have been reported.[20,21] In this study, we were able to assign the group vibrational modes of $MGeO_4$ (M = Zr, Hf) through shifts of the Raman bands in a $Hf_{1-x}Zr_xGeO_4$ solid solution series and through the application of the Raman polarization selection rules to micro-Raman spectra of single crystals. Macro-Raman spectra of undoped and titanium-activated $MGeO_4$ powder samples and micro-Raman spectra of single crystals of $ZrGeO_4$:Ti^{4+} confirm that Ti^{4+} occupies the Ge^{4+} site in $ZrGeO_4$ and in $HfGeO_4$. In addition, we find that whereas all of the modes most affected by Ti^{4+} doping are those arising from the GeO_4^{4-} group, not all of the GeO_4^{4-} modes are strongly affected by Ti^{4+} doping. Specifically, we conclude that Ti^{4+} substitution for Ge^{4+} significantly affects Raman bands arising from rotational and bending motions of the GeO_4^{4-} group about the *c*-axis, within the *ab*-plane. We apply group and molecular orbital theory to explain this effect.

Experimental Section

Powder diffraction patterns were obtained with an Enraf Nonius FR552 Guinier camera with Cu $K\alpha_1$ radiation. Films were digitized using a scanning densitometer, and lattice parameters determined by the least-squares method with a modified version of the Novak and Colville[22] templates.

The details of the preparation of the solid solution $Hf_{1-x}Zr_xGeO_4$:Ti samples have been described.[23] The samples were prepared from aqueous solutions containing the appropriate molar ratios of $HfOCl_2 \cdot 8H_2O$ and $ZrOCl_2 \cdot 8H_2O$ (Teledyne Wah Chang Albany; RGS), and either $(NH_4)_2TiO(C_2O_4)_2 \cdot H_2O$ (Johnson-Matthey), or an aqueous $TiCl_4$ (20% HCl, Aldrich) solution, as the Ti^{4+} source. GeO_2 (Eagle-Picher, 99.999%) was added as a solid, and the coprecipitation attained through the slow addition of concentrated ammonium hydroxide. After collection, washing, and drying at 95 °C, the amorphous hydrous metal oxide gel was normally combined with a Li_2SO_4 (Johnson-Matthey, 99.7%) flux, and fired in an alumina crucible in air at 1100 °C for 6 h.[24] The resulting ingot was washed in hot distilled water to remove the flux.

Powder diffraction of the collected and dried material showed only the scheelite phase, with linear changes in lattice parameters across each solid solution series. Elemental analysis of the $HfGeO_4$:Ti samples showed complete incorporation of Ti^{4+}, with no significant flux impurities.[25]

The single crystals were prepared from a $Li_2MoO_4 \cdot 2MoO_3$ flux containing 2 wt % ZrO_2 and 5-fold excess of GeO_2. Titanium was added as TiO_2 at 100 and 200 mol % of the ZrO_2 value. Platinum crucibles were used, and the charges were cooled at a rate of 4 °C/h from 1300 to 900 °C in a vertical molybdenum disilicide tube furnace. The molten charges were air-quenched from 900 °C, and the crystals extracted after treatment with hot water and hot concentrated ammonium hydroxide solution. The crystals were of high optical quality, usually assuming the crystal habit shown in Figure 1, and ranged in size from 0.5 to 1.0 mm.

Larger crystals of $ZrGeO_4$ (up to 5 mm) were grown using the technique of accelerated crucible rotation[26] (ACRT) in combination with a 1 °C/h cooling rate. The lattice parameters observed for increasing titanium levels are consistent with those found in $ZrGeO_4$:Ti^{4+} powder samples. By comparison with similar cell volume changes in the $HfGeO_4$:Ti^{4+} series, the crystals prepared with 100 and 200 mol % TiO_2 addition have, respectively, ∼4 and ∼12 mol % Ti^{4+} incorporation. Energy-dispersive X-ray analysis of two of the high Ti^{4+} content crystals indicated 8−9 mol % Ti^{4+} incorporation and no significant molybdenum incorporation.[25]

Macro-Raman spectra of the powder samples were obtained using a SPEX 1403 double monochromator with 1800 grooves/mm holographically ruled gratings. The detector is a high-sensitivity GaAs photocathode RCA C31034 photomultiplier tube. Spectra of powder samples held in melting point capillaries were obtained from a 90° scattering configuration using 100 mW of 488.0 nm excitation, measured at the sample. Spectra were generated by scanning from 100 to 1000 cm^{-1} in 1.0 cm^{-1} increments at 2.0 s integration time with the slits set to 200 μm/280 μm/280 μm/200 μm.

Micro-Raman spectra were obtained using an Instruments SA S3000 spectrometer with 488.0 nm excitation in conjunction with an EEV Class One #15-11 CCD detector, and slits set to 200 μm/4.09 mm/200 μm. Also, scanned spectra were acquired using 647.1 nm excitation in conjunction with a Hamamatsu R943-02 photomultiplier tube (PMT) with the slits set to 400 μm/480 μm/480 μm/400 μm. The spectra obtained with the CCD were acquired over a 10 s read time, whereas those obtained using the PMT were acquired by scanning from 100 to 900 cm^{-1} in 1.0 cm^{-1} increments at 2.0 s integration time. Micro-Raman spectroscopy was performed by focusing the laser beam with an Olympus MS Plan 50 (0.80

(11) Pope, S. J. A.; West, Y. D. *Spectrochim. Acta Part A* **1995**, *51*, 2027.
(12) Porto, S. P. S.; Scott, J. F. *Phys. Rev.* **1967**, *157*, 716.
(13) Scott, J. F. *J. Chem. Phys.* **1968**, *48*, 874.
(14) Hardcastle, F. D.; Wachs, I. E. *J. Raman Spectrosc.* **1995**, *26*, 397.
(15) Hanuza, J.; Maczka, M.; Macalik, L.; van der Maas, J. *J. Mol. Struct.* **1994**, *325*, 119.
(16) Hanuza, J.; Benzar, A.; Haznar, A.; Macska, M.; Pietraszko, A.; van der Maas, J. H. *Vibr. Spectrosc.* **1996**, *12*, 25.
(17) Ramakrishnan, V.; Arul Dhas, G.; Narayanan, P. S. *J. Raman Spectrosc.* **1986**, *17*, 273.
(18) Miller, S. A.; Rast, H. E.; Caspers, H. H. *J. Chem. Phys.* **1970**, *52*, 4172.
(19) Zhang, X. X.; Schulte, A.; Chai, B. H. T. *Solid State Commun.* **1994**, *89*, 181.
(20) Michel, D.; Van Den Borre, M. T.; Ennaciri, A. *Adv. Ceram.* **1988**, *24A* (Sci. Technol. Zirconia 3), 555.
(21) Vandenborre, M. T.; Michel, D.; Ennaciri, A. *Spectrochim. Acta A* **1989**, *45A*, 721.
(22) Novak, G. A.; Colville, A. A. *Am. Mineral.* **1989**, *74*, 488.
(23) Lambert, P. M., submitted to *Inorg. Chem.*
(24) The $ZrGeO_4$:0.025 Ti sample was fired with 11 wt % Li_2MoO_4 (Aesar, 99%).
(25) Teledyne Wah Chang Albany, Analytical Laboratory Services.
(26) Scheel, H. J.; Schulz-Dubois, E. O. *J. Cryst. Growth* **1971**, *8*, 304.

NA) objective at various positions on the ⟨001⟩ and ⟨103⟩ faces of the $ZrGeO_4$ and $ZrGeO_4$:Ti^{4+} single crystals. The laser polarization remained fixed relative to the optical instrumentation; the crystal orientation relative to the incident polarization was controlled using a microscope rotational stage.

Results and Discussion

The transition-metal germanates, $MGeO_4$ (here M = Zr or Hf), are tetragonal and belong to the C_{4h} crystal point group. The irreducible representations of the optical phonons derived from a group theoretical treatment are

$$\Gamma_{optical} = 3A_g(R) + 5B_g(R) + 5E_g(R) + 4A_u(IR) + 3B_u(inactive) + 4E_u(IR) \quad (1)$$

where IR, R, and inactive represent infrared active, Raman active, and inactive modes, respectively. Furthermore, site group analysis predicts the following external translational and librational modes:

$$\Gamma_{trans} = \Gamma_{Zr} + \Gamma_{Ge} = 2B_g(R) + 2E_g(R) + 2A_u(IR) + 2E_u(IR) \quad (2)$$

$$\Gamma_{lib} = A_g(R) + E_g(R) + B_u(inactive) + E_u(IR) \quad (3)$$

$$\Gamma_{ext} = \Gamma_{trans} + \Gamma_{lib} = A_g(R) + 2B_g(R) + 3E_g(R) + 2A_u(IR) + B_u(inactive) + 3E_u(IR) \quad (4)$$

The remaining internal modes can be attributed to the vibrational motions of the GeO_4 group:

$$\Gamma_{int} = \Gamma_{optical} - \Gamma_{ext} = 2A_g(R) + 3B_g(R) + 2E_g(R) + 3A_u(IR) + 2B_u(inactive) + 2E_u(IR) \quad (5)$$

The polarizability tensors for the Raman active modes are:

$$A_g = \begin{pmatrix} a & 0 & 0 \\ 0 & a & 0 \\ 0 & 0 & b \end{pmatrix}, \quad B_g = \begin{pmatrix} c & d & 0 \\ d & -c & 0 \\ 0 & 0 & 0 \end{pmatrix}, \quad E_g = \begin{pmatrix} 0 & 0 & e \\ 0 & 0 & f \\ e & f & 0 \end{pmatrix}, \begin{pmatrix} 0 & 0 & -f \\ 0 & 0 & e \\ -f & -e & 0 \end{pmatrix} \quad (6)$$

Our study included Raman analyses of both powders and single crystals of $ZrGeO_4$ and Ti^{4+}-doped $ZrGeO_4$. A Raman spectrum obtained from a powder sample of $ZrGeO_4$ is shown in Figure 2. The spectrum is comparable to those published in previous reports, although some of our band assignments differ from those of Vandenborre and co-workers.[20,21] (We will address this later in the paper.) The inset in Figure 2 shows portions of $ZrGeO_4$ and $ZrGeO_4$:Ti^{4+} (2.5%) spectra. Certain Raman bands of $ZrGeO_4$:Ti^{4+} (2.5%) powder are clearly shifted relative to the corresponding bands of $ZrGeO_4$. Of those shown here, the band at 293 cm^{-1} is strongly shifted whereas the band at 305 cm^{-1} is only modestly so. Other bands, such as that at 255 cm^{-1}, show no movement with Ti^{4+} doping. The $ZrGeO_4$ Raman bands most affected by Ti^{4+} doping, manifested as band shifts in the $ZrGeO_4$:Ti^{4+} (2.5%) powder spectrum, are at 294, 378, 406, and 565 cm^{-1}. Presumably the bands affected are those whose vibrational modes involve the site occupied by Ti^{4+}. One of the primary goals of this research was to identify the site occupancy of Ti^{4+}-doped metal germanates. Therefore, a correct assignment of the vibrational modes is crucial to the determination of Ti^{4+} site occupancy.

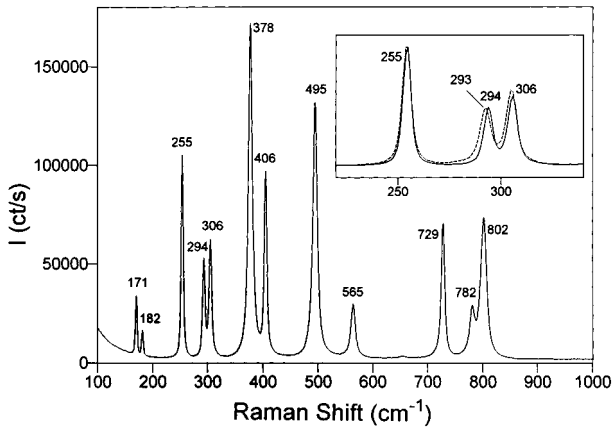

Figure 2. Powder Raman spectrum of $ZrGeO_4$. The inset shows a portion of spectra of $ZrGeO_4$ (solid) and $ZrGeO_4$:Ti^{4+} (2.5%) (dashed).

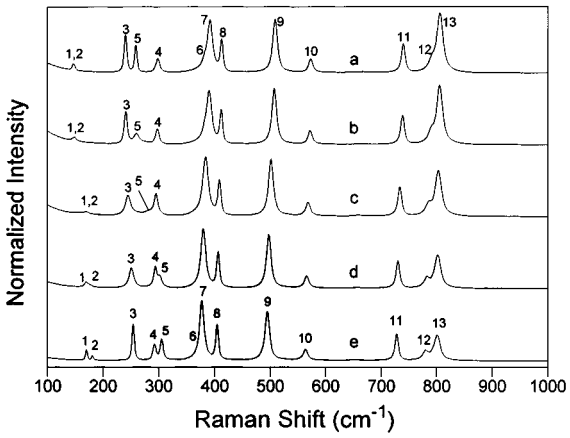

Figure 3. Raman spectra of the $Hf_{1-x}Zr_xGeO_4$ solid solution series: (a) $x = 0$; (b) $x = 0.1$; (c) $x = 0.5$; (d) $x = 0.8$; (e) $x = 1.0$.

$Hf_{1-x}Zr_xGeO_4$ Solid Solution Series. One approach that we have taken to assign the group vibrational modes of $ZrGeO_4$ is through shifts of the Raman bands in a $Hf_{1-x}Zr_xGeO_4$ solid solution. Raman spectra of a $Hf_{1-x}Zr_xGeO_4$ solid solution series are shown in Figure 3. The 13 Raman bands of $ZrGeO_4$ have been numbered to more easily follow their shift as the stoichiometry progresses from $ZrGeO_4$ to $HfGeO_4$. In general, the external modes can be expected to appear at lower wavenumbers, whereas the internal modes can be found at higher wavenumbers. Inspection of Figure 3 reveals that some bands shift to lower wavenumbers as Hf^{4+} is substituted for Zr^{4+}, whereas others shift to higher wavenumbers. For example, in the region below 450 cm^{-1} we see that bands 1, 2, 3, and 5 shift to lower wavenumbers as the stoichiometry progresses from $ZrGeO_4$ to $HfGeO_4$; however, bands 4 and 6−13 shift to higher wavenumbers. Plots of the Raman band shifts as a function of $Hf_{1-x}Zr_xGeO_4$ chemical composition are shown in Figure 4a,b.

The band shifts can be explained by changes in atomic mass and chemical bonding force constants. The atomic mass of Zr is 91.2, whereas that of Hf is 178.5. Therefore, those Raman bands due to external modes involving M should shift to lower wavenumbers upon

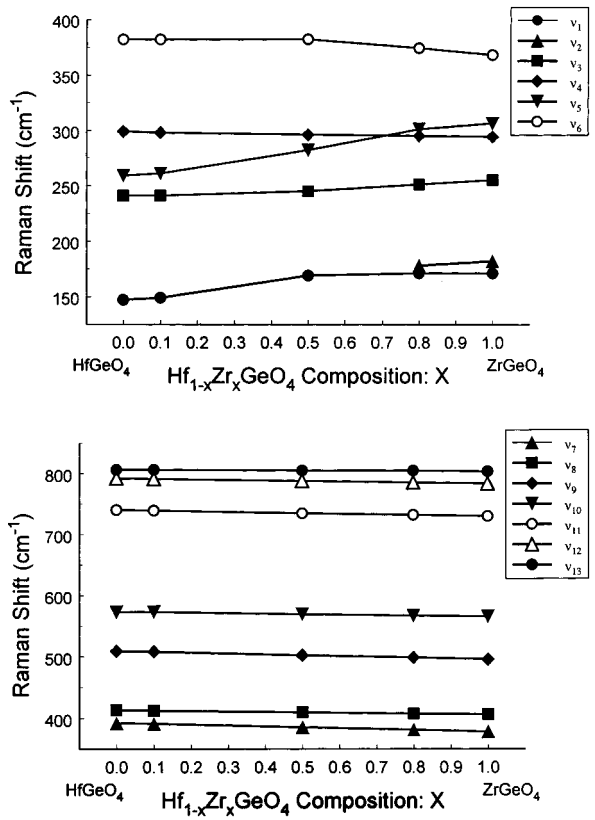

Figure 4. Plots of Raman shift as a function of stoichiometry for (a) Γ_{ext} and (b) Γ_{int}.

substitution of Hf^{4+} for Zr^{4+}. Given that the mass of Ge at 72.6 is significantly lower than that of Zr, we can expect that the two lowest wavenumber bands, 1 and 2 in Figure 3, constitute the Γ_M (M = Zr, Hf) mode set. Here we assume that the magnitude of any increases in the bond strengths, and therefore the vibrational force constants, of the MO_8 group are offset by the more significant change in mass accompanying the substitution of Hf^{4+} for Zr^{4+}. Also, we can expect that any changes in bond strengths of the MO_8 group would also affect the Γ_{Ge} bands as well. The ν_3 and ν_5 bands, which we attribute to Γ_{Ge}, also shift to lower wavenumbers upon substitution of Hf^{4+} for Zr^{4+}. The net result of M substitution is that all four of the Γ_{trans} bands shift to lower wavenumbers. We justify our assignment of ν_1 and ν_2 as Γ_M and ν_3 and ν_5 as Γ_{Ge} based on the mass argument described above. Furthermore, the greater Raman scattering strength (greater polarizability) of ν_3 and ν_5 relative to that of ν_1 and ν_2 is indicative of greater covalency, which we would expect for the GeO_4^{4-} group. The ν_4 and ν_6 bands, which shift to higher wavenumbers upon substitution of Hf^{4+} for Zr^{4+}, can be attributed to Γ_{lib}, thereby completing our assignment of Γ_{ext}. The remaining bands, ν_7 through ν_{13}, constitute the set of Γ_{int}. A complete assignment of the group modes for $ZrGeO_4$ is shown in Table 1.

A shift to lower wavenumbers can be expected for Γ_M bands as Hf^{4+} is substituted for Zr^{4+}. However, the mass change accompanying the metal substitution would not have the same direct effect on vibrational modes associated with the GeO_4^{4-} group. The effect of the substitution of Hf^{4+} for Zr^{4+} on vibrational modes associated with the GeO_4^{4-} group is a slight shifting of the Γ_{int} bands to higher wavenumbers. In the GeO_4^{4-} group, changes in vibrational force constants would now

Table 1. Assignment of Group Modes from $Hf_{1-x}Zr_xGeO_4$ Solid Solutions[a,b]

mode assignment	Raman band (cm^{-1})	mode assignment	Raman band (cm^{-1})
Γ_{Zr}	171 (ν_1)	Γ_{int}	406 (ν_8)
Γ_{Zr}	182 (ν_2)	Γ_{int}	495 (ν_9)
Γ_{Ge}	255 (ν_3)	Γ_{int}	565 (ν_{10})
Γ_{lib}	294 (ν_4)	Γ_{int}	729 (ν_{11})
Γ_{Ge}	306 (ν_5)	Γ_{int}	782 (ν_{12})
Γ_{lib}	368 (ν_6)	Γ_{int}	802 (ν_{13})
Γ_{int}	378 (ν_7)		

[a] The numbers in parentheses are the band numbers from Figure 3. [b] The Raman band shifts are for $ZrGeO_4$ only.

Table 2. Mode Assignment of $ZrGeO_4$ Bands Most Affected by Ti^{4+} Doping

$\tilde{\nu}$ (cm^{-1})	mode assignment
294 (ν_4)	Γ_{lib} (GeO_4)
378 (ν_7)	Γ_{int} (GeO_4)
406 (ν_8)	Γ_{int} (GeO_4)
565 (ν_{10})	Γ_{int} (GeO_4)

be the dominant factor affecting Raman band shifts because the constituent atoms, and therefore their masses, remain the same. That the vibrational force constants for the GeO_4^{4-} group should be greater in $HfGeO_4$ than in $ZrGeO_4$ is reasonable given the slightly smaller cell volume, and presumably shorter bond lengths, of $HfGeO_4$. (The cell volumes of $ZrGeO_4$ and $HfGeO_4$ are 249.5 and 246.8 Å^3, respectively.) Accordingly, we have qualitatively characterized the Γ_{int} Raman bands as arising primarily from the GeO_4^{4-} groups.

The group mode assignments of the Raman bands most affected by Ti^{4+} are shown in Table 2. All of the modes most affected by Ti^{4+} doping are those arising from the GeO_4^{4-} group, strongly suggesting that Ti^{4+} occupies the Ge^{4+} site. An interesting aspect of the results is that whereas all of the modes most affected by Ti^{4+} doping are those arising from the GeO_4^{4-} group, not all of the GeO_4^{4-} modes are equally affected by Ti^{4+} doping. We address and explain this particular point later in the paper. Also, in a later section we will discuss the results obtained by polarized micro-Raman spectroscopy and show that the band assignments based upon the series of $Hf_{1-x}Zr_xGeO_4$ solid solutions are consistent with those based upon the application of the Raman polarization selection rules to single crystals of $MGeO_4$. Furthermore, the polarized micro-Raman results will also point to the Ge^{4+} site as the one occupied by the Ti^{4+} dopant.

It is worthwhile to elaborate on the value of a solid solution series in properly making Raman band assignments. Note that whereas ν_1 and ν_2 are clearly resolved in the spectrum of $ZrGeO_4$, they are not resolved in the spectrum of $HfGeO_4$ and could easily be incorrectly assigned as a single band. Likewise, an even more subtle example is the combination of ν_6 and ν_7. The deconvolved ν_6 and ν_7 from the spectrum of $HfGeO_4$ appear at 382.0 and 392.0 cm^{-1} and have 100% and 55% Lorentzian (45% Gaussian) line shape, respectively (Figure 5). Band deconvolution was performed on the remainder of the spectral set, holding constant the percent Lorentzian character for each band as determined by the results of the operation on $HfGeO_4$. The results of that operation are shown in Table 3.

The trend that we observe is that band separation decreases with mixing of the metals and in fact achieves

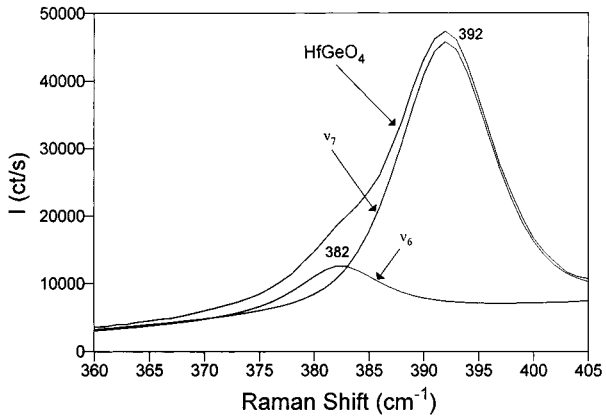

Figure 5. Deconvolution of ν_6 and ν_7 from $HfGeO_4$.

Table 3. Band Deconvolution from $Hf_{1-x}Zr_xGeO_4$ Solid Solutions

compound	ν_6 (cm^{-1})	ν_7 (cm^{-1})	I_6/I_7[a]
$HfGeO_4$	382	392	0.212
$Hf_{0.9}Zr_{0.1}Ge_{O4}$	382	391	0.231
$Hf_{0.5}Zr_{0.5}GeO_4$	382	385	0.459
$Hf_{0.2}Zr_{0.8}GeO_4$	374	381	0.245
$ZrGeO_4$	368	378	0.056

[a] I represents the integrated intensity under the band.

its lowest value of 3 cm^{-1} for $Hf_{0.5}Zr_{0.5}GeO_4$. As stoichiometry is again achieved, at $ZrGeO_4$ the band separation is 10 cm^{-1}, the same as that for $HfGeO_4$. However, notice that the value of the relative intensities of ν_6 and ν_7, I_6/I_7, has reached its lowest level in $ZrGeO_4$. Consequently, the moderate shoulder present in the $HfGeO_4$ spectrum is absent in that of $ZrGeO_4$, and so ν_6 can easily go undetected. Without the solid solution series, ν_6 could not readily be detected in the $ZrGeO_4$ spectrum, and the observed number of bands would fall one short of the number predicted by group theory.

The changes in the band separation of ν_6 and ν_7 and their relative intensities (I_6/I_7) are noteworthy given that ν_6 and ν_7 have been assigned to Γ_{lib} and Γ_{int}, respectively, and that the librational modes have been attributed to rotational motions of the GeO_4^{4-} group.[13] Inspection of Figure 3 reveals that ν_4, the other member of the set constituting Γ_{lib}, does not show a decrease in relative intensity comparable to that of ν_6 with compositional change from $Hf_{0.5}Zr_{0.5}GeO_4$ to $ZrGeO_4$.

Powder samples of $HfGeO_4$ doped with 1, 2, 4, and 6% Ti^{4+} were prepared, and Raman spectra of the entire set were acquired for comparison with those obtained from $ZrGeO_4$:Ti^{4+}. As observed in the spectra of $ZrGeO_4$:Ti^{4+}, some $HfGeO_4$:Ti^{4+} bands are moderately shifted, some strongly shifted, and others show no movement with Ti^{4+} doping. All of the aforementioned effects can be seen in the partial spectra shown in Figure 6. There is no movement of ν_3 with Ti^{4+} doping, whereas ν_5 shows modest movement and ν_4 is strongly shifted. Also, ν_4 manifests a greater intensity change relative to ν_3 than does ν_5. Plots of $HfGeO_4$ and $HfGeO_4$:Ti^{4+} (6%) in the spectral region corresponding to the region in the $ZrGeO_4$ spectrum most affected by Ti^{4+} doping are shown in Figure 7. The bands are labeled for easy comparison with the $ZrGeO_4$:Ti^{4+} data. We find that the $HfGeO_4$ bands affected by Ti^{4+} doping correspond to the most strongly affected $ZrGeO_4$:Ti^{4+} bands, and these are listed in Table 4. As for $ZrGeO_4$:Ti^{4+}, we again observe that all of the modes most

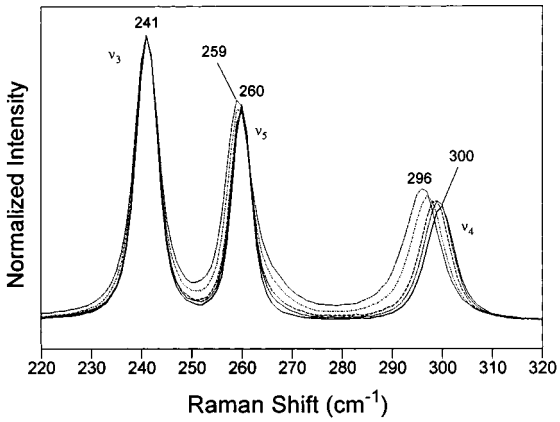

Figure 6. Powder Raman spectra of $HfGeO_4$ (solid), $HfGeO_4$:Ti^{4+} (1%) (dotted), $HfGeO_4$:Ti^{4+} (2%) (dashed), $HfGeO_4$:Ti^{4+} (4%) (dash−dot), and $HfGeO_4$:Ti^{4+} (6%) (dash−dot−dot).

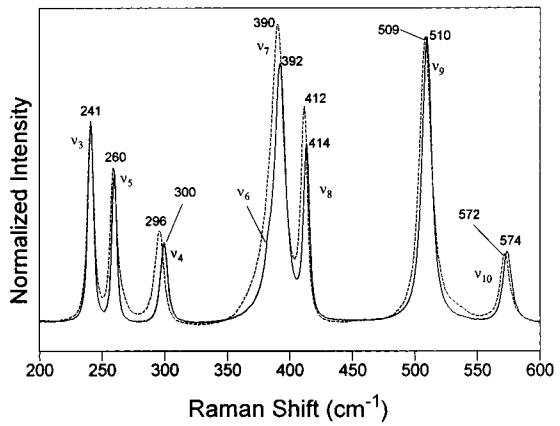

Figure 7. Powder Raman spectra of $HfGeO_4$ (solid) and $HfGeO_4$:Ti^{4+} (6%) (dashed).

Table 4. Mode Assignment of $MGeO_4$ Bands Most Affected by Ti^{4+} Doping

$HfGeO_4$ $\tilde{\nu}$ (cm^{-1})	$ZrGeO_4$ $\tilde{\nu}$ (cm^{-1})	mode assignment
300 (ν_4)	294 (ν_4)	Γ_{lib} (GeO_4)
392 (ν_7)	378 (ν_7)	Γ_{int} (GeO_4)
414 (ν_8)	406 (ν_8)	Γ_{int} (GeO_4)
574 (ν_{10})	565 (ν_{10})	Γ_{int} (GeO_4)

affected by Ti^{4+} doping are those arising from the GeO_4^{4-} group, consistent with Ti^{4+} occupying the Ge^{4+} site in $ZrGeO_4$ and in $HfGeO_4$. It is noteworthy that, in $HfGeO_4$ as well as in $ZrGeO_4$, not all of the bands arising from GeO_4^{4-} vibrational motions are equally affected by Ti^{4+} doping. We address this point in the following section by first identifying the symmetries of all the bands constituting the $MGeO_4$ Raman spectrum.

Polarized Micro-Raman Spectroscopy of $ZrGeO_4$:Ti^{4+} Crystals. The application of the Raman polarization selection rules to single crystals of $MGeO_4$ simplifies the task of vibrational mode assignment. Single crystals of $ZrGeO_4$, $ZrGeO_4$:Ti^{4+} (∼4%), and $ZrGeO_4$:Ti^{4+} (∼12%) were grown with a crystal defined by the ⟨001⟩, ⟨103⟩, and ⟨101⟩ faces. Micro-Raman spectra of the ⟨103⟩ faces of $ZrGeO_4$ and $ZrGeO_4$:Ti^{4+} single crystals are shown in Figure 8. These crystals were more heavily doped than the previously discussed powder, and so manifest even more dramatic spectral changes. The most significant shifts occur for the bands at ($ZrGeO_4$ wavenumbers) 294, 378, 405, and 564 cm^{-1}. Also, a band emerges at 647 cm^{-1} with Ti^{4+} doping. This band is apparently the very weak one at 655 cm^{-1} in

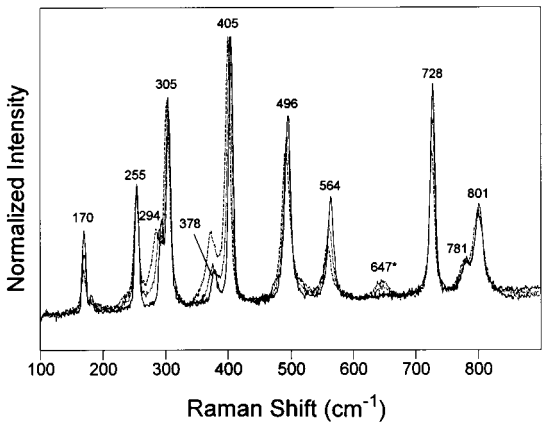

Figure 8. Micro-Raman spectra of the ⟨103⟩ faces of $ZrGeO_4$ (solid), $ZrGeO_4$:Ti^{4+} (∼4%) (dotted), and $ZrGeO_4$:Ti^{4+} (∼12%) (dashed). Band positions are of $ZrGeO_4$ except for the 647 cm^{-1} band. The incident polarization is perpendicular to the *c*-axis.

the $ZrGeO_4$ powder spectrum, and is apparently forbidden when probing the ⟨103⟩ face. As we observed in the $ZrGeO_4$:Ti^{4+} (2.5%) powder spectrum, Ti^{4+} doping does not cause all the bands to shift strongly. Those bands which show modest or no discernible shift are at 170, 255, 305, 496, 728, 781, and 801 cm^{-1}. Those Raman bands from the ⟨103⟩ face that are most affected with respect to band shift are at 294, 378, 405, and 564 cm^{-1}. That only some of the bands shift as a result of Ti^{4+} doping suggests that Ti^{4+} is not indiscriminately positioned but rather preferentially occupies specific lattice sites. Last, we note that in addition to band shifts, changes in relative intensities are observed with Ti^{4+} doping, thereby indicating changes in chemical bond polarizability. The spectra in Figure 8 are all normalized to the most intense band at 405 cm^{-1}. Relative to the 405 cm^{-1} band then, the intensities of those bands at 170, 496, 564, and 728 cm^{-1} decrease, whereas those at 378 and 647 cm^{-1} increase. The relative strengths of bands at 255, 294, 305, 781, and 801 cm^{-1} remain unchanged. We will comment further on the changes in relative intensity later.

It is not possible to employ group theory in conjunction with polarized Raman analysis of powders to assign Raman bands because secondary and tertiary reflections from the powder generate a depolarized signal. That is not the case for single crystals with smooth, highly reflective faces. Therefore, polarized micro-Raman spectra of a prudently selected single crystal face in conjunction with a powder spectrum allows us to accurately assign the symmetries of the Raman bands. The identification of the symmetries of the bands most affected by Ti^{4+} doping provides insight into the changes in chemical bonding induced by doping. The Raman polarizability tensors in eq 6 suggest that a polarized Raman analysis of the ⟨001⟩ face of a single crystal should allow us to identify the symmetries of all the Raman bands of a powder spectrum. Specifically, using the backscattering configuration, the A_g mode can only be detected from the ⟨001⟩ face when the analyzer is parallel to the incident polarization. Raman scattering from the A_g mode is forbidden for perpendicular polarization. Also, because the tensor elements α_{xx} and α_{yy} (a) are equal, the intensity of the A_g band should not vary with orientation within the *XY* plane. See eqs 7 and 8. (Our terminology is such that the *X*, *Y*, and *Z* axes of the Raman tensors correspond to the *a*, *b*, and *c* crystallographic axes of $MGeO_4$.) The element α_{zz}, although it may be different from α_{xx} and α_{yy}, cannot be probed in this orientation. Conversely, the B_g modes can be detected with parallel or crossed polarizers, the relative intensities of the two configurations being dependent upon the orientation of the incident polarization. For example, if the incident electric field is polarized parallel to the *X*-axis, then having the analyzer in the parallel position probes the α_{xx} tensor element (c), whereas the analyzer positioned perpendicular will probe the α_{xy} tensor element (d). Rotating the crystal 45° within the ⟨001⟩ plane transforms the B_g tensor as shown in eqs 7 and 8. At 45°, the analyzer parallel configuration probes the original α_{xy} tensor element (d) and the analyzer perpendicular configuration probes the original α_{xx} tensor element (c). Finally, the E_g modes are forbidden in this experimental orientation, and therefore should not appear in any spectra of the ⟨001⟩ face. All three vibrational mode symmetries can be differentiated then by probing the ⟨001⟩ face in the backscattering arrangement.

$$A_g^0 = \begin{pmatrix} a & 0 & 0 \\ 0 & a & 0 \\ 0 & 0 & b \end{pmatrix} \qquad B_g^0 = \begin{pmatrix} c & d & 0 \\ d & -c & 0 \\ 0 & 0 & 0 \end{pmatrix} \tag{7}$$

$$A_g^{45} = \begin{pmatrix} a & 0 & 0 \\ 0 & a & 0 \\ 0 & 0 & b \end{pmatrix} \qquad B_g^{45} = \begin{pmatrix} d & -c & 0 \\ -c & -d & 0 \\ 0 & 0 & 0 \end{pmatrix} \tag{8}$$

Parallel and perpendicularly polarized micro-Raman spectra of the ⟨001⟩ face of a $ZrGeO_4$ single crystal are shown in Figure 9. The incident beam was polarized parallel to one of the ordinary (*X* or *Y*) axes of the crystal. Therefore, in this orientation, the A_g bands will be allowed only with the analyzer parallel, but the B_g bands should be allowed in both the parallel and perpendicular configurations. For the experimental results to be in perfect agreement with predictions based on Raman polarization selection rules would require exact alignment of the crystal relative to the incident beam. The crystals analyzed here were not cut and polished and crystal alignment for the micro-Raman study was performed by eye under the microscope. Therefore, some misalignment of the crystal is expected and with it some deviation of the spectra from that expected for a perfectly aligned ⟨001⟩ face. Consequently, we expect some "leakage" from bands that are nominally forbidden for a given crystal orientation and polarization. The bands at 294, 378, and 802 cm^{-1} are assigned to A_g symmetry. All three of these bands show far greater intensity in the parallel versus the perpendicular configuration. The 378 cm^{-1} band from the ⟨001⟩ face is considerably weaker than that of the powder spectrum, and so one could identify it as a forbidden E_g mode "leaking" through due to misalignment, as is the case at 255 and 495 cm^{-1}. However, note that the "leaked" E_g modes at 255 and 495 cm^{-1} have comparable intensities for parallel and perpendicular configurations, whereas the 378 cm^{-1} band in the parallel configuration is far stronger than that from the perpendicular arrangement. The reason for the weakness of the 378 cm^{-1} band detected from the ⟨001⟩ face is that the α_{zz} tensor element is apparently significantly greater than $\alpha_{xx,yy}$; i.e., $b \gg a$. The bands at 294, 378, and 802 cm^{-1} account for all three of the Raman-active A_g modes of

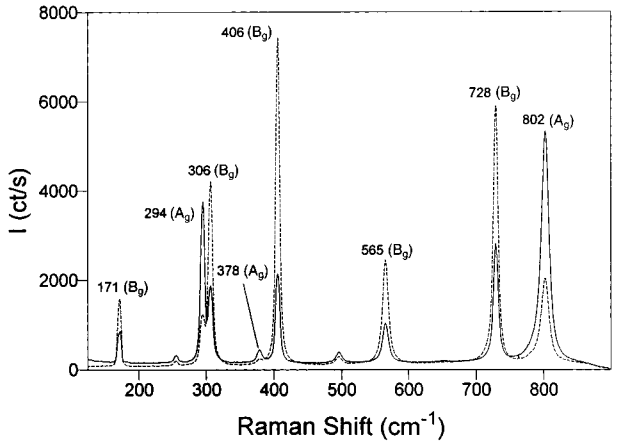

Figure 9. Micro-Raman spectrum of the ⟨001⟩ face of a $ZrGeO_4$ single crystal. The incident polarization is parallel to one of the ordinary (*X* or *Y*) axes of the crystal. Analyzer parallel (solid), analyzer perpendicular (dashed).

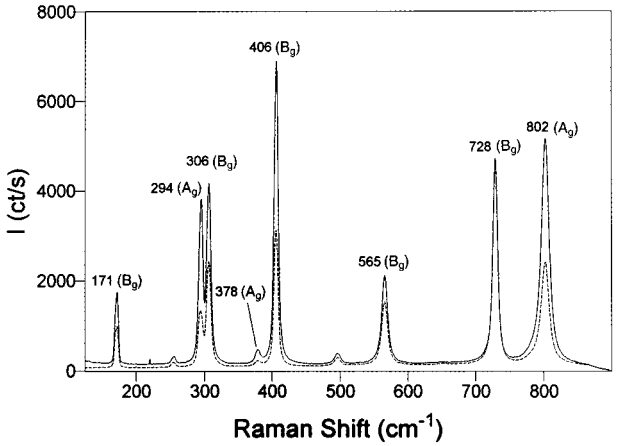

Figure 10. Micro-Raman spectrum of the ⟨001⟩ face of a $ZrGeO_4$ single crystal. The incident polarization is 45° with respect to one of the ordinary (*X* or *Y*) axes of the crystal. Analyzer parallel (solid), analyzer perpendicular (dashed).

$ZrGeO_4$. The remaining bands at 171, 306, 406, 565, and 729 cm^{-1} are assigned B_g symmetry. That all these bands are more intense in the perpendicular configuration is strong evidence for the B_g assignment. Furthermore, the different parallel vs perpendicular intensity ratios (I_{par}/I_{perp}) for those five bands manifest the different relative tensor element values (*c*/*d*) in the different modes, and only B_g modes can do that in this orientation. The bands at 171, 306, 406, 565, and 729 cm^{-1} account for all five of the Raman-active B_g modes of $ZrGeO_4$. Therefore, by a process of elimination, the remaining two unassigned bands observed in the powder spectrum at 182 and 782 cm^{-1}, along with the two leaked bands at 255 and 495 cm^{-1}, must be assigned a symmetry of E_g. That gives us four E_g bands, one band short of the number of modes predicted by group theory. The final E_g band must be ν_6 at 368 cm^{-1}, which we identified through our study of the $Hf_{1-x}Zr_xGeO_4$ solid solutions.

Spectra obtained from the ⟨001⟩ face rotated 45° with respect to the original ordinary axis and within the ⟨001⟩ plane are shown in Figure 10 and confirm the above assignments. The bands at 294, 378, and 802 cm^{-1} show the same parallel/perpendicular response as for the experimental arrangement with the incident polarization parallel to an ordinary axis. The invariability of I_{par}/I_{perp} with rotation of the ⟨001⟩ face is the expected response for vibrational modes of A_g symmetry. Conversely, the bands at 171, 306, 406, 565, and 728 cm^{-1} have different parallel/perpendicular responses from those observed at 0°. At 45° orientation their $I_{par}/I_{perp} \geq 1$, whereas at 0° their $I_{par}/I_{perp} \leq 1$. This response pattern is consistent with the transformation of the B_g tensor through a 45° rotation. Finally, the two weak bands at 255 and 495 cm^{-1} have comparable parallel and perpendicular intensities, the same as observed at the 0° orientation. So their response is consistent with our assignment of them as E_g bands that have "leaked through".

Table 5. Raman Band Assignments of $ZrGeO_4$[a]

this work		Vandenborre et al.[21]	
$\tilde{\nu}$ (cm^{-1})	sym	$\tilde{\nu}$ (cm^{-1})	sym
171 (ν_1)	B_g	176	E_g
182 (ν_2)	E_g	186	B_g
		202	E_g
255 (ν_3)	E_g	259	A_g
294 (ν_4)	A_g	298	B_g
306 (ν_5)	B_g	311	E_g
368 (ν_6)	E_g		
378 (ν_7)	A_g	382	B_g
406 (ν_8)	B_g	410	A_g
495 (ν_9)	E_g	500	E_g
565 (ν_{10})	B_g	569	B_g
729 (ν_{11})	B_g	732	E_g
782 (ν_{12})	E_g	786	B_g
802 (ν_{13})	A_g	806	A_g

[a] The numbers in parentheses are the band numbers from Figure 3.

Our assignments of the $ZrGeO_4$ Raman bands are summarized in Table 5. We have included the assignments of Vandenborre and co-workers for comparison. The assignments of Vandenborre et al. were made based upon a normal-coordinate analysis and the Raman spectrum of $ZrGeO_4$ powder. Comparison of our powder Raman spectrum with that of Vandenborre et al. reveals good agreement with respect to the number and relative intensities of almost all the bands; they are nearly identical. However, we differ on the assignment of some of the mode symmetries and the identification of ν_6 at 368 cm^{-1}. In addition, we observe a band at 655 cm^{-1}, not seen by Vandenborre and co-workers, which we attribute to an impurity or defect because of its weakness and the already complete assignment of 13 Raman-active modes. Also, Vandenborre and co-workers report a band at 202 cm^{-1}, which we cannot detect. Clearly, the most significant disagreement is not with the detection of $ZrGeO_4$ Raman bands but with their assignments.

Returning to the subject of Ti^{4+} site occupancy, we observe that the Raman bands most affected by Ti^{4+} doping are at 294, 378, 406, and 565 cm^{-1}. We find that these bands, listed in Table 6, constitute a set whose vibrational mode symmetries are consistent with those predicted by eqs 3 and 5 for a librational mode and three internal modes of the GeO_4^{4-} group. Furthermore, our mode assignment based on the symmetry of the affected bands is consistent with that in Table 2 based on the study of the $Hf_{1-x}Zr_xGeO_4$ solid solutions. By having correctly assigned the symmetries of the $MGeO_4$ Raman bands, including those bands most affected by Ti^{4+} doping, the nature of the Ti^{4+} chemical bonding at the Ge^{4+} lattice site can be more fully characterized. We

Table 6. Mode and Symmetry Assignments of Raman Bands from ⟨103⟩ Face of $ZrGeO_4$ Most Affected by Ti^{4+} Doping[a]

$\tilde{\nu}$ (cm^{-1})	mode assignment	sym assignment
294 (ν_4)	Γ_{lib} (GeO_4)	A_g
378 (ν_7)	Γ_{int} (GeO_4)	A_g
406 (ν_8)	Γ_{int} (GeO_4)	B_g
565 (ν_{10})	Γ_{int} (GeO_4)	B_g

[a] The numbers in parentheses are the band numbers from Figure 3.

Table 7. Correlation Diagram for the GeO_4^{4-} Ion in the $MGeO_4$ Crystal

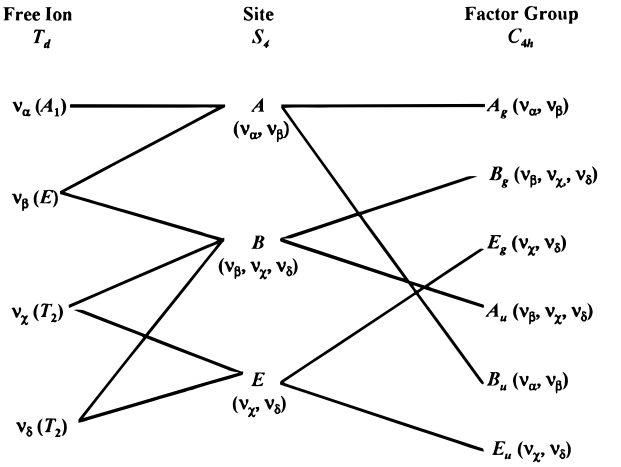

Table 8. Correlation of GeO_4^{4-} Internal Modes with Td Free Ion

normal vibration	T_d free ion	C_{4h} crystal
sym str	A_1 (ν_α)	A_g (ν_α) + B_u (ν_α)
sym bend	E (ν_β)	A_g (ν_β) + B_u (ν_β)
		B_g (ν_β) + A_u (ν_β)
asym str	T_2 (ν_χ)	B_g (ν_χ) + A_u (ν_χ)
		E_g (ν_χ) + E_u (ν_χ)
asym bend	T_2 (ν_δ)	B_g (ν_δ) + A_u (ν_δ)
		E_g (ν_δ) + E_u (ν_δ)

noted earlier, in the $Hf_{1-x}Zr_xGeO_4$ solid solutions section, that whereas all of the modes most affected by Ti^{4+} doping are those arising from the GeO_4^{4-} group, not all of the GeO_4^{4-} modes are strongly affected by Ti^{4+} doping. Here we apply group and molecular orbital theory to explain this effect.

Note that the affected bands have two common characteristics; i.e., that their Raman tensors have nonzero α_{xx} and α_{yy} tensor elements and that they can be assigned to GeO_4^{4-} rotation or Ge−O bending motions within the *ab*-plane. The Γ_{lib} mode in Table 6 is a GeO_4^{4-} rotation. We assign the Γ_{int} bands in Table 6 to Ge−O bending motions based on the application of the site group method to correlate the S_4 site symmetry species to a XY_4 free molecule of T_d symmetry. The correlation diagram for the GeO_4^{4-} ion in the $ZrGeO_4$ crystal is shown in Table 7. The free GeO_4^{4-} ion with T_d symmetry has four normal vibrational modes consisting of A_1 (ν_α) symmetric stretch, E (ν_β) symmetric bend, T_2 (ν_χ) asymmetric stretch, and T_2 (ν_δ) asymmetric bend. The symmetry of the free GeO_4^{4-} ion is lowered to S_4 in the crystal, and the free ion T_d modes can be correlated to the internal modes of the factor group C_{4h} $MGeO_4$ crystal. That correlation of the T_d local vibrational modes to C_{4h} phonons is shown in Table 8. In our assignment and correlation of $ZrGeO_4$ bands to local T_d modes, we expect the stretching modes to constitute the highest energy phonons in the spectrum, and indeed the bands at 729 (ν_{11}, B_g), 782 (ν_{12}, E_g), and 802 (ν_{13}, A_g) cm^{-1} have the appropriate symmetries to correlate to ν_χ (B_g), ν_χ (E_g), and ν_α (A_g), respectively. Referring to Tables 1 and 5, we see that the remaining Γ_{int} bands are at 378 (ν_7, A_g), 406 (ν_8, B_g), 495 (ν_9, E_g), and 565 cm^{-1} (ν_{10}, B_g), which by symmetry correlate to ν_β (A_g), ν_β (B_g), ν_δ (E_g), and ν_δ (B_g), respectively. Of those four Γ_{int} bands, the A_g and B_g modes are among those most affected by Ti^{4+} doping. In fact, the bands listed in Table 6 as those most affected by Ti^{4+} doping constitute the entire set of combined A_g and B_g bending and rotational modes for $ZrGeO_4$. There is one E_g bending mode and one E_g rotational mode, both of which are not as strongly affected by Ti^{4+} doping. Note, however, that the nonzero E_g tensor elements are α_{xz}, α_{zx}, α_{yz}, and α_{zy}. In contrast, the strongly affected A_g and B_g modes have nonzero α_{xx}, α_{yy}, or α_{xy} (α_{yx}) tensor elements. Therefore, we conclude that Ti^{4+} substitution for Ge^{4+} significantly affects Raman bands arising from rotational and bending motions of the GeO_4^{4-} group about the *c*-axis, within the *ab*-plane.

Here we offer an explanation for the effects of Ti^{4+} doping on the Raman spectra of $ZrGeO_4$ and $HfGeO_4$. The tetrahedral GeO_4^{4-} group is formed by a combination of the oxygen orbitals and sp^3 hybridized atomic orbitals from Ge^{4+}. However, if Ti^{4+} is substituted for Ge^{4+}, the atomic orbitals of the central atom are no longer sp^3 hybridized. The 4s (a_1), 4p (t_2), 3d (e), and 3d (t_2) atomic orbitals of Ti^{4+} will, in a tetrahedral coordination, transform to the molecular orbitals a_1, t_2, e, and t_2, respectively. For simplification, we will ignore the distortion at the Ge^{4+} site from ideal tetrahedral geometry. One a_1 and three t_2 molecular orbitals form σ-bonding orbitals in the tetrahedral structure. In particular, note that the t_2 bonding orbitals are formed by a hybridization of Ti^{4+} d (t_2) and p (t_2) orbitals. The 3d (e) atomic orbitals would transform to e nonbonding molecular orbitals. However, metal oxides readily form π bonds, and the 3d (e) orbitals can form π-bonding orbitals with the ligand in a tetrahedral structure. The excitation of luminescence from Ti^{4+} may be due to a ligand to metal charge-transfer absorption involving a π (e) back-bonding orbital. If π bonding does occur, then the local electronic structure of the TiO_4^{4-} tetrahedron is significantly different from that of the sp^3 hybridized GeO_4^{4-} tetrahedron. In particular, we could expect the $d_{x^2-y^2}$ (e) orbital involved in π bonding to hinder rotation of TiO_4^{4-} in the *ab*-plane, thereby damping lattice vibrational modes related to the unhindered rotation of the sp^3-hybridized GeO_4^{4-} tetrahedron. Consequently, Raman bands arising from "GeO_4^{4-} rotations" should shift and perhaps broaden to lower wavenumber, which is what we observe.

Regarding our interpretation of the spectroscopic effects of Ti^{4+} occupancy of the Ge^{4+} site, it is important to remember that the Raman bands of the $MGeO_4$ spectrum are due to lattice vibrations, phonons, and are not due to local vibrational modes. Therefore, we have to consider TiO_4^{4-} tetrahedra not in terms of a local motion that produces a discrete band but rather as a point defect perturbing a lattice vibration. In that capacity, one thinks of TiO_4^{4-} point hindered rotations causing specific lattice vibrations, those involving the

rotation or bending of the GeO_4^{4-} group, to function like a damped oscillator. The manifestation of such an effect should be a shifting and broadening of the Raman band to lower wavenumber.

Conclusion

Raman spectroscopy has been used to probe the chemical bonding and crystal structure of $MGeO_4:Ti^{4+}$, an efficient X-ray phosphor. The group vibrational modes of $MGeO_4$ have been assigned based on the movements of the Raman bands in a $Hf_{1-x}Zr_xGeO_4$ solid solution series and through the application of the Raman polarization selection rules to micro-Raman spectra of single crystals. A comparison of the band assignments made by each method reveals that the same results are obtained by either the application of Raman polarization selection rules to single crystals of $ZrGeO_4$ or through the study of $Hf_{1-x}Zr_xGeO_4$ solid solutions. Thus, we have an internally consistent method for assigning Raman bands to functional groups or substructures in the metal germanates. Furthermore, we have applied the results of our band assignment study to determine the site occupancy of transition metal dopants, in this case Ti^{4+}, in metal germanates. Macro-Raman spectra of undoped and titanium-activated $ZrGeO_4$ and $HfGeO_4$ powder samples and micro-Raman spectra of single crystals of $ZrGeO_4:Ti^{4+}$ confirm that Ti^{4+} occupies the Ge^{4+} site in $ZrGeO_4$ and in $HfGeO_4$.

We find that whereas all of the modes most affected by Ti^{4+} doping are those arising from the GeO_4^{4-} group, not all of the GeO_4^{4-} modes are strongly affected by Ti^{4+} doping. Specifically, we conclude that Ti^{4+} substitution for Ge^{4+} significantly affects Raman bands arising from the rotational and bending motions of the GeO_4^{4-} group about the *c*-axis, within the *ab*-plane. We propose an explanation for this effect based on group and molecular orbital theory. When Ti^{4+} is substituted for Ge^{4+} the atomic orbitals of the central atom are no longer sp^3 hybridized, and the 3d (e) orbitals can form π-bonding orbitals with the ligand in a tetrahedral structure. If π bonding does occur, then the local electronic structure of the TiO_4^{4-} tetrahedron is significantly different from that of the sp^3-hybridized GeO_4^{4-} tetrahedron. In particular, we could expect the $d_{x^2-y^2}$ (e) orbital involved in π bonding to hinder rotation of TiO_4^{4-} in the *ab*-plane, thereby damping lattice vibrational modes related to the unhindered rotation of the sp^3 hybridized GeO_4^{4-} tetrahedron.

Acknowledgment. P.M.L. would like to thank G.S. Jarrold for his help in sample preparation. Figure 1 was produced with ATOMS by shape software.

CM970205F